01 Jan 2005

Calibration and Compensation of Near-Field Scan Measurements

Masahiro Yamaguchi

Richard E. DuBroff
Missouri University of Science and Technology, red@mst.edu

Kevin P. Slattery

Michael A. Cracraft

et. al. For a complete list of authors, see https://scholarsmine.mst.edu/ele_comeng_facwork/1476

Recommended Citation

M. Yamaguchi et al., "Calibration and Compensation of Near-Field Scan Measurements," *IEEE Transactions on Electromagnetic Compatibility*, Institute of Electrical and Electronics Engineers (IEEE), Jan 2005.
The definitive version is available at https://doi.org/10.1109/TEMC.2005.853165

Calibration and Compensation of Near-Field Scan Measurements

Jin Shi, *Student Member, IEEE*, Michael A. Cracraft, *Student Member, IEEE*, Kevin P. Slattery, *Senior Member, IEEE*, Masahiro Yamaguchi, *Member, IEEE*, and Richard E. DuBroff, *Senior Member, IEEE*

***Abstract*—A procedure for the calibration and compensation of near-field scanning is described and demonstrated. Ultimately, the objective is to quantify the individual field components associated with electromagnetic interference (EMI) from high speed circuitry and devices. Specific examples of these methods are shown. The effects of compensation are small but noticeable when the uncompensated output signal from near field scanning is already a very good representation of the field being measured. In other cases, the improvement provided by compensation can be significant when the uncompensated output signal bears little resemblance to the underlying field.**

***Index Terms*—Calibration, compensation, near-field probes, near-field scanning.**

I. Introduction

NEAR-FIELD scanning measurements are increasingly being used to provide information regarding the electric and magnetic fields in the vicinity of integrated circuit (IC) chips and printed circuit boards [1]. A noncontact IC surface near-field measurement also provides a means to analyze the current distribution over the chip package. This information may be helpful in diagnosing EMI problems created by sources on the chip [2]. Ideally, these measurements should simultaneously exhibit excellent resolution, high sensitivity, and should not disturb the field being measured [3]. One of the initial probe correction approaches was proposed by Kerns [4]–[6] in 1963. Plane wave scattering matrix theory was used to characterize the receiving properties of a near field probe. This approach assumes multiple interactions between the probe and device under test (DUT) are neglected. The theory of probe compensated near-field measurement by applying the Lorentz reciprocity theorem was described by Paris *et al*. [7] and applied to the problem of determining antenna characteristics including the far-field pattern. More recently formulations of probe corrected planar near-field scanning in both frequency and time domains have been proposed by Hansen and Yaghjian [8], [9]. The present work described herein is an application of this theory to the problem of characterizing EMI through the use of near-field scanning measurements.

Manuscript received February 16, 2004; revised February 22, 2005.

J. Shi is with Intel Corporation, Santa Clara, CA 95053 USA.

M. A. Cracraft is with the Electromagnetic Laboratory, University of Missouri, Rolla, MO 65409 USA.

K. P. Slattery is with the Mobility Group, Intel Corporation, Hillsboro, OR 97124 USA.

M. Yamaguchi is with Tohoku University, Sendai 980-8579, Japan.

R. E. DuBroff is with the Electrical and Computer Engineering Department, University of Missouri, Rolla MO 65409 USA (e-mail: red@umr.edu).

Digital Object Identifier 10.1109/TEMC.2005.853165

In many cases, the output of the near-field probe is simply regarded as being directly proportional to the field intensity at the location of the probe. This does not allow for the fact that the presence of the probe itself may introduce some perturbation in the quantity (field component) being measured. In addition, the probe may have directional characteristics which manifest themselves in terms of a probe output that is determined by more than one field component.

The main purpose of this paper is to develop a procedure for the calibration of near field scanning probes. This calibration determines the probe's receiving characteristics. The characteristics, in turn, can be used to correct for (compensate) the effects of the probe in making near field measurements. In this way, the true unperturbed fields that would have existed in the absence of the probe could be extracted from the probe's near-field measurements.

To examine these limitations more closely, full wave simulations are compared with measurements to show an example of the tradeoff between probe size, sensitivity, and resolution in Section II. Section II also contains a discussion of the field perturbations caused by the proximity between the near-field probe and the DUT. This part is based entirely on full wave simulation.

In Section III, we describe a procedure of calibration and compensation for a probe. A well characterized, precisely manufactured probe is used to produce a reference field. The response of a somewhat imprecise handmade probe to this reference field is used to deduce a characterization (calibration) of this handmade probe. This characterization, in turn, provides the basis for the probe compensation. The procedure is demonstrated by using different handmade probes to observe the near-field components produced by a known structure. The fields calculated based on these measurements, with and without calibration, are then compared with the fields predicted by full wave simulations and with analytical predictions by quasistatic expressions [10]. The experimental results are presented in Section IV, and the conclusions are presented in Section V.

II. Influence of the Probe on Near-Field Measurements

The probes considered in this section all consist of a segment of semirigid coaxial cable terminated in a closed loop. For simplicity these probes will be referred to as magnetic field probes even though their outputs may technically be functions of both the electric and magnetic fields. In general, smaller probes will introduce less disturbance in the field components being measured, but will also have less sensitivity [3]. A set of three such

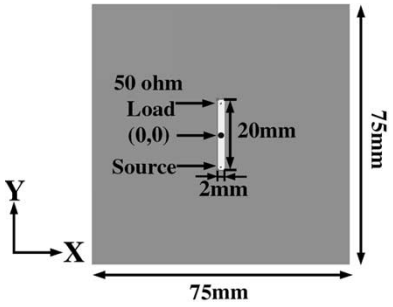

Fig. 1. Top view of a microstrip structure.

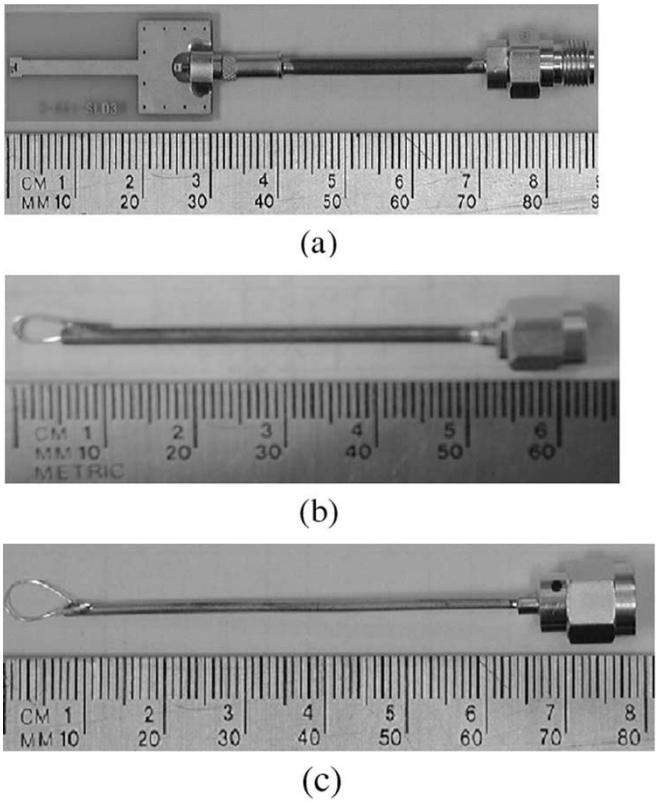

Fig. 2. Magnetic field probes. (a) Square aperture, 1mm by 0.2 mm. (b) Small elliptical aperture, 5 mm by 3.5 mm. (c) Larger elliptical aperture, 8 mm by 5 mm.

probes having various dimensions was used to observe the fields produced by the microstrip trace shown in Fig. 1.

The three magnetic field probes used to observe the fields produced by this structure are shown in Fig. 2.

The first probe, shown in Fig. 2(a), was manufactured on a printed circuit board (PCB) and has a rectangular loop aperture. The remaining two probes were made by hand. The loop apertures are roughly elliptical and the aperture sizes shown in the figure refer to the major and minor axis lengths. The microstrip structure, shown in Fig. 1, was driven through port 1 of an HP8753D vector network analyzer (VNA), and in each case the appropriate probe was mounted on a computer controlled positioner. The probe output was connected to port 2 of the VNA. The computer controlled positioner was programmed for a square scanning grid of 51 equally spaced steps in the x

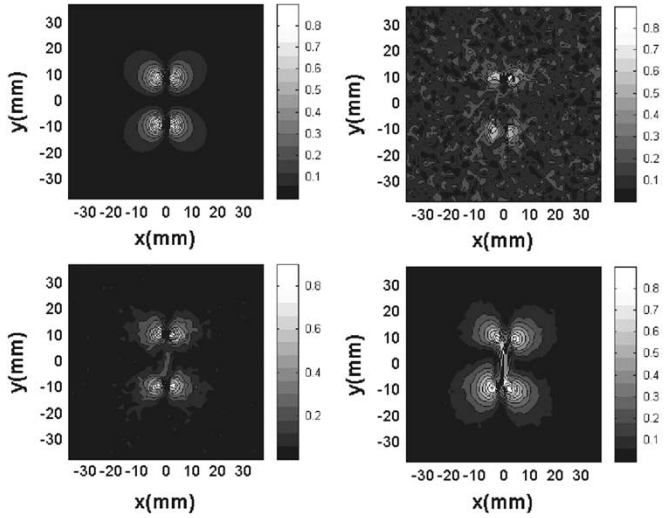

Fig. 3. A comparison of measured data for the three magnetic field probes. Upper left: results from a finite difference time domain (FDTD) simulation; Upper right: results from the probe in Fig. 2(a); Lower left: results from the probe in Fig. 2(b); Lower right: results from the probe in Fig. 2(c).

and y directions. The total scan plane area was set to 76.5 mm by 76.5 mm with a vertical standoff distance of approximately 1 mm between the lowest point of the probe and the microstrip trace. For the purpose of making comparisons between measurements from different probes as well as comparisons with full wave simulations, all of the probes were considered to be oriented in the y direction (i.e., the normal direction to the loop aperture was parallel to the microstrip trace shown in Fig. 1). The measured and simulated results, for a frequency of 100 MHz, are shown in Fig. 3.

The result shown in the upper left panel is the simulated value of the y component of the magnetic field. The results in the remaining panels are the magnitudes of S_{21}. In order to compensate for the varying degrees of sensitivity, each plot has been normalized to display a maximum value of 1 on a linear scale. The direct simulation (upper left) shows the best resolution and exhibits no obvious random noise-like pattern. The upper right panel, in contrast shows comparable resolution but the effects of background noise are apparent. As the loop aperture increases further in size (lower left and lower right panels) the noise becomes less noticeable but at the same time the resolution seems less sharp. In particular, at a point above the middle of the microstrip trace $(x = y = 0)$, the y-component of the magnetic field should be approximately zero. This agrees with the upper left panel, but not with the lower right panel.

While this set of figures suggests a tradeoff between resolution and probe size, there is also another possible effect that involves the perturbation of the field due to the presence of the probe. To examine this effect, numerical full wave simulations were used to consider the effect of the probe on the field components being measured [10]. A commercially available transmission line matrix (TLM) method simulation was run for the fields produced by a microstrip trace in the presence of a coaxial conductor. The purpose of the coaxial conductor was to model the probe as a 10 mm long hollow square outer conductor

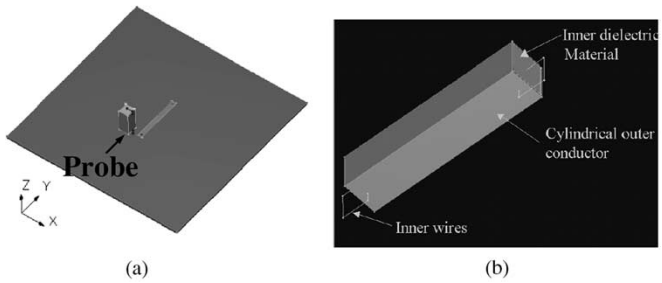

Fig. 4. Geometric structures included in the TLM simulation. (a) Geometrical relationship between the probe and the microstrip. (b) Closeup view of the probe as modeled in the TLM simulation.

having a cross section of 4 mm by 4 mm. This outer conductor, in turn, surrounded an inner filamentary conductor and dielectric material. At one end, the outer and inner conductors were modeled as being joined with a filamentary wire to form a rectangular loop. At the other end, the inner and outer conductors were modeled as being connected through a finite impedance of 50 Ohms. The vertical stand-off distance between the probe and the printed circuit board was modeled as 3 mm in this case. The geometric structures included in the numerical simulation are shown in Fig. 4.

If the probe is not included in the simulation, the microstrip structure is quite symmetrical and would be expected to produce a field distribution that displays a commensurate degree of symmetry. The magnitudes of the x, y, and z components of the simulated magnetic field with and without the probe are shown in Fig. 5.

The first row of Fig. 5 shows the x, y, and z components of the undisturbed magnetic field produced by the microstrip trace acting alone. The second row includes the microstrip trace and the probe. Small changes in the field component can be seen. In order to make these changes more obvious, the difference between the first and second rows is shown in the third row for the x, y, and z components, respectively.

III. Calibration and Compensation Procedures

Consider a magnetic field of frequency ω, propagating in free space, and let the plane wave component of the magnetic field at a horizontal wave vector of $\vec{k}_h = k_x\hat{x} + k_y\hat{y}$ be expressed as $\vec{H}_0(\omega, \vec{k}_h)$ [7], [11], [12]. The contribution of this particular plane wave component to the magnetic field at some spatial point, $\vec{r}$, is then given by

$$d\vec{H}(\vec{r}\,|\,\omega, \vec{k}_h) = \vec{H}_0(\omega, \vec{k}_h)e^{-j(k_x x + k_y y + \gamma z)}\frac{d^2\vec{k}_h}{2\pi} \quad (1)$$

where

$$\gamma = \begin{cases} \sqrt{\omega^2\mu\varepsilon - k_h^2}, & k_h^2 \le \omega^2\mu\varepsilon \\ -j\sqrt{k_h^2 - \omega^2\mu\varepsilon}, & k_h^2 > \omega^2\mu\varepsilon \end{cases}$$

$$\vec{r} = x\hat{x} + y\hat{y} + z\hat{z}, \quad k_h^2 = \left|k_h^2\right| = k_x^2 + k_y^2$$

$$d\vec{k}_h = dk_x dk_y.$$

Now consider a probe located so that a fixed reference point on the probe is at the coordinate system origin. Following the approach described in [8], the response of this probe to a monochromatic plane wave component can be expressed as a linear combination of the x, y, and z components of $d\vec{H}(\vec{r}\,|\,\omega, \vec{k}_h)$ so that the corresponding contribution to the probe's output can be expressed as

$$dp(\vec{r}\,|\,\omega, \vec{k}_h)|_{\vec{r}=0} = \vec{R}(\omega, \vec{k}_h) \cdot \vec{H}_0(\omega, \vec{k}_h)\frac{d^2\vec{k}_h}{2\pi}. \quad (2)$$

The linear combination coefficients contained within the vector $\vec{R}(\omega, \vec{k}_h)$ characterize the response of the probe, and the calibration procedure to be described subsequently consists of determining these linear combination coefficients.

Therefore, considering the scan plane to correspond to $z = 0$ and denoting the position vector of a fixed reference point on the probe by $\vec{r}_h = x\hat{x} + y\hat{y}$, the probe's output can be expressed as

$$dp(\vec{r}_h\,|\,\omega, \vec{k}_h) = \vec{R}(\omega, \vec{k}_h) \cdot \vec{H}_0(\omega, \vec{k}_h)e^{-j\vec{k}_h \cdot \vec{r}_h}\frac{d^2\vec{k}_h}{2\pi}. \quad (3)$$

Finally, using the superscripts x and y to designate two different orientations of the probe

$$\begin{bmatrix} dp^x(\vec{r}_h\,|\,\omega, \vec{k}_h) \\ dp^y(\vec{r}_h\,|\,\omega, \vec{k}_h) \end{bmatrix} = \begin{bmatrix} \vec{R}^x(\omega, \vec{k}_h) \\ \vec{R}^y(\omega, \vec{k}_h) \end{bmatrix} \cdot \vec{H}_0(\omega, \vec{k}_h)e^{-j\vec{k}_h \cdot \vec{r}_h}\frac{d^2\vec{k}_h}{2\pi} \quad (4)$$

from which

$$\begin{bmatrix} p^x(\vec{r}_h\,|\,\omega) \\ p^y(\vec{r}_h\,|\,\omega) \end{bmatrix} = \iint \begin{bmatrix} \vec{R}^x(\omega, \vec{k}_h) \\ \vec{R}^y(\omega, \vec{k}_h) \end{bmatrix} \cdot \vec{H}_0(\omega, \vec{k}_h)e^{-j\vec{k}_h \cdot \vec{r}_h}\frac{d^2\vec{k}_h}{2\pi}. \quad (5)$$

The quantities on the left side represent the probe outputs (in two different orientations) as a function of the probe's spatial position in the scan area and therefore represent experimental measurements.

In order to obtain the probe characteristics contained within $\vec{R}^x(\omega, \vec{k}_h)$, for example, the calibration procedure is then as follows.

1) Connect a radiating structure that produces a known magnetic field plane wave spectrum $\vec{H}_0^{(1)}(\omega, \vec{k}_h)$ at a given angular frequency and record the probe output values as $p_1^x(\vec{r}_h\,|\,\omega)$.
2) Connect a different radiating structure that produces a known magnetic field plane wave spectrum, $\vec{H}_0^{(2)}(\omega, \vec{k}_h)$, at a given angular frequency and record the probe output values as $p_2^x(\vec{r}_h\,|\,\omega)$ while keeping the probe orientation unchanged.

As described in [8], the linear combination vector, $\vec{R}^x(\omega, \vec{k}_h)$, is nonunique since for any given value of $(\omega, \vec{k}_h)$ the magnetic field plane wave component satisfies $(\vec{k}_h + \gamma\hat{z}) \cdot \vec{H}_0(\omega, \vec{k}_h) = 0$. Consequently adding any constant multiple of $(\vec{k}_h + \gamma\hat{z})$ to $\vec{R}^x(\omega, \vec{k}_h)$ will have no effect in (5), i.e.: $[\vec{R}^x(\omega, \vec{k}_h) + 2(\vec{k}_h + \gamma\hat{z})] \cdot \vec{H}_0(\omega, \vec{k}_h) = \vec{R}^x(\omega, \vec{k}_h) \cdot \vec{H}_0(\omega, \vec{k}_h)$. To enable a unique solution for the three unknown linear combination coefficients in $\vec{R}^x(\omega, \vec{k}_h)$, the constraint $(\vec{k}_h + \gamma\hat{z}) \cdot$

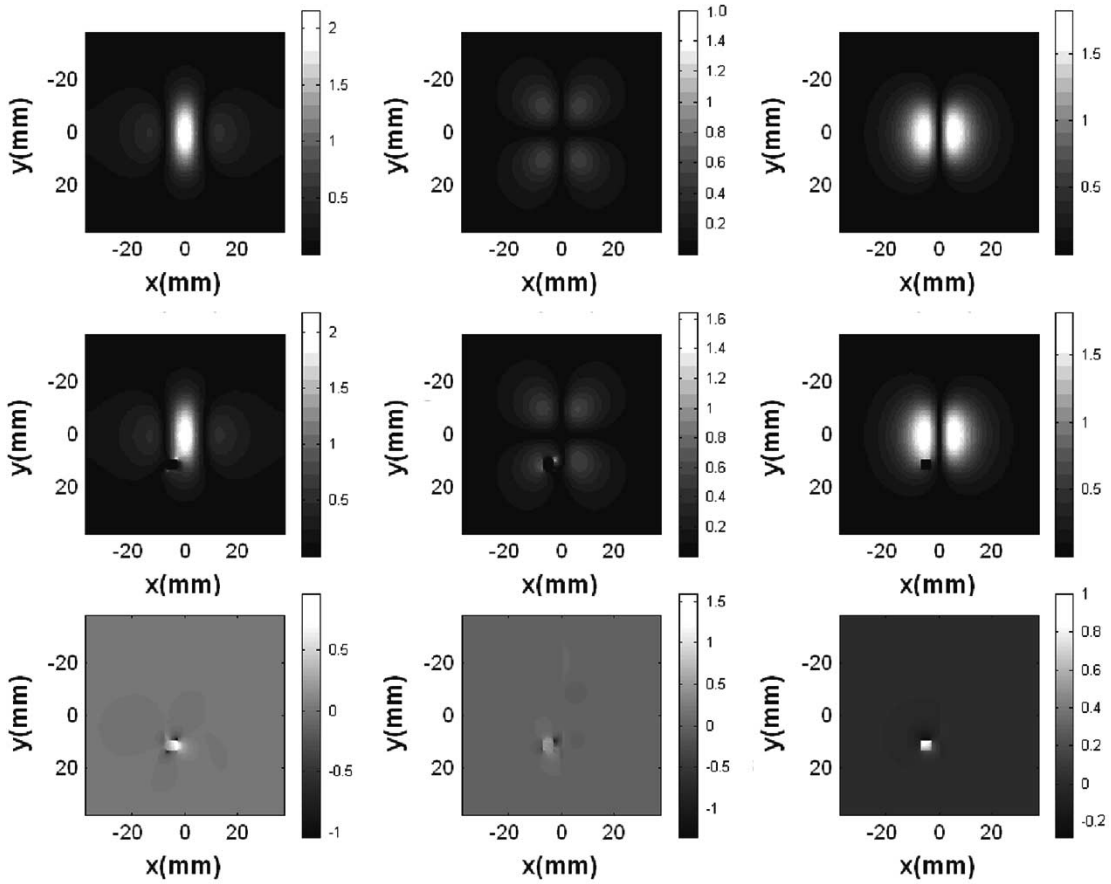

Fig. 5. TLM simulations showing small local magnetic field perturbations caused by the presence of the probe. First row: The x, y, and z components of the simulated magnetic field when the probe was not included. Second row: The x, y, and z components of the simulated magnetic field when the probe was included. Third row: Difference between the first and second rows.

$\vec{R}^x(\omega, \vec{k}_h) = 0$ is imposed. Similarly in the case of $\vec{R}^y(\omega, \vec{k}_h)$ a constraint of $(\vec{k}_h + \gamma\hat{z}) \cdot \vec{R}^y(\omega, \vec{k}_h) = 0$ is imposed.

3) The recorded measurements, $p_1^x(\vec{r}_h \,|\, \omega)$ and $p_2^x(\vec{r}_h \,|\, \omega)$, are then Fourier transformed from the $\vec{r}_h$ domain to the $\vec{k}_h$ domain. Since the probes are moved in discrete spatial steps, this data transformation is actually accomplished by using a two dimensional discrete Fourier transform.
4) After the data has been transformed into the frequency-wave number domain the individual linear combination coefficients in $\vec{R}^x(\omega, \vec{k}_h)$ are found from the simultaneous solution of

$$\begin{bmatrix} p_1^x\left(\omega, \vec{k}_h\right) \\ p_2^x\left(\omega, \vec{k}_h\right) \\ 0 \end{bmatrix} = \begin{bmatrix} H_{0x}^1(\omega, \vec{k}_h) & H_{0y}^1(\omega, \vec{k}_h) & H_{0z}^1(\omega, \vec{k}_h) \\ H_{0x}^2(\omega, \vec{k}_h) & H_{0y}^2(\omega, \vec{k}_h) & H_{0z}^2(\omega, \vec{k}_h) \\ k_x & k_y & \gamma \end{bmatrix} \times \begin{bmatrix} R_x^x(\omega, \vec{k}_h) \\ R_y^x(\omega, \vec{k}_h) \\ R_z^x(\omega, \vec{k}_h) \end{bmatrix} \tag{6}$$

A similar procedure is followed to determine the linear combination coefficients contained in $\vec{R}^y(\omega, \vec{k}_h)$.

Once the probe has been adequately characterized by determining $\vec{R}^x(\omega, \vec{k}_h)$ and $\vec{R}^y(\omega, \vec{k}_h)$, the effect of the probe can be removed from subsequent measurements made over a different source (compensation). The steps involved in compensation for the magnetic field produced by an unknown device under test (DUT) are as follows:

1) Using the same set of probe orientations, measure and record the probe output as a function of spatial position in the scan aperture at a fixed frequency of ω.
2) Transform the measurements, $p^x(\vec{r}_h \,|\, \omega)$ and $p^y(\vec{r}_h \,|\, \omega)$ from the spatial domain to the wave number domain.
3) Solve the system of equations

$$\begin{bmatrix} p^x(\omega, \vec{k}_h) \\ p^y(\omega, \vec{k}_h) \end{bmatrix} = \begin{bmatrix} \vec{R}^x(\omega, \vec{k}_h) \\ \vec{R}^y(\omega, \vec{k}_h) \end{bmatrix} \cdot \vec{H}_0(\omega, \vec{k}_h) \tag{7}$$

together with the constraint: $(\vec{k}_h + \gamma\hat{z}) \cdot \vec{H}_0(\omega, \vec{k}_h) = 0$ for the plane wave spectrum of the magnetic field $\vec{H}_0(\omega, \vec{k}_h)$.

For the experimental results shown in the next section, the radiating structure used to calibrate the smaller hand built probes was actually a large square loop probe. The two sets of calibration fields, $\vec{H}_0^{(1)}(\omega, \vec{k}_h)$ and $\vec{H}_0^{(2)}(\omega, \vec{k}_h)$, were provided by

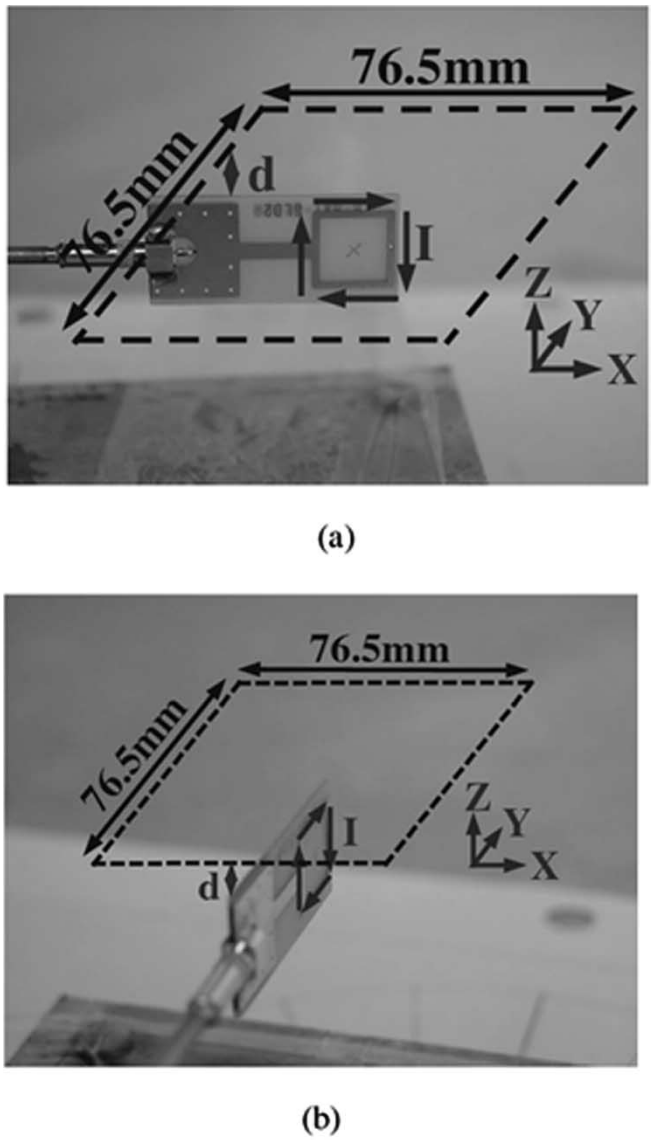

Fig. 6. Two different orientations of the calibration source. (a) A square loop current flowing in the xz plane. (b) A square loop current flowing in the yz plane.

using the same radiating structure in two different orientations, as shown in Fig. 6(a) and (b).

A quasi-static approximate expression, described in [10], was used to provide the values of the calibration fields.

IV. Experimental and Numerical Results

Fig. 7 compares the results of a full wave (FDTD) simulation, uncompensated measurements, and compensated measurements for the y component of the magnetic field produced by the microstrip trace of Fig. 1. The gray scale plots in this and all subsequent figures have been normalized to a maximum value of 1.

A second example was obtained by replacing the microstrip structure with a square loop in a horizontal plane. The scan area and spatial sampling interval were the same as in the previous microstrip example. The coordinate origin was taken as the center of the scan area and it was intended that the center of the

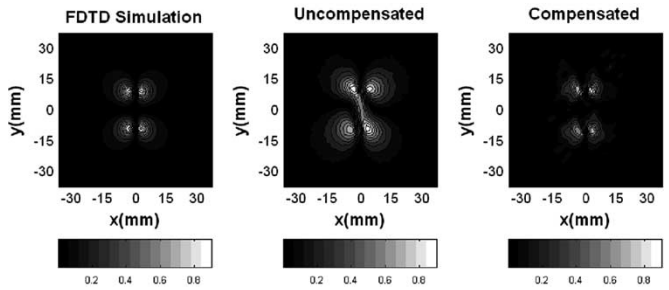

Fig. 7. The effects of probe compensation on the measurement of H_y. (FDTD simulation: the magnitude of H_y from full wave numerical FDTD simulation; Uncompensated: the magnitude of S_{21} obtained directly from VNA measurements of the probe's output; Compensated: the magnitude of H_y as calculated by the compensation procedure.)

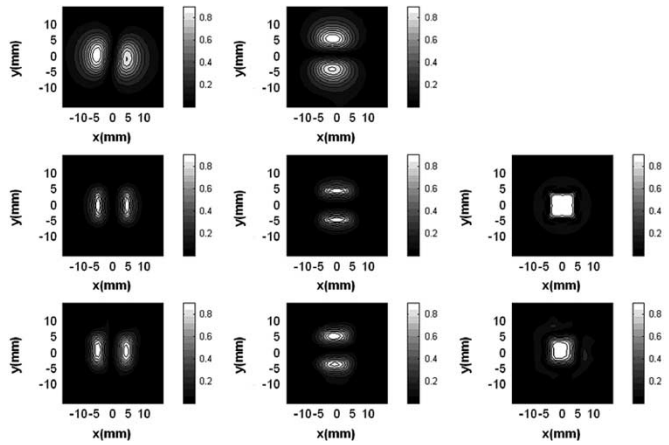

Fig. 8. Compensation results for the magnetic field components produced by a square loop using a magnetic field probe. Top row: $|S_{21}|$ for probes oriented in the x and y directions. Middle row: magnitude of the magnetic field components in the x, y, and z directions as calculated by an analytical approximation [10]. Third row: magnitude of the magnetic field components in the x, y, and z directions determined by applying probe compensation to the measurements in the first two rows.

square current loop should be directly beneath the center of the scan area with the sides of the square current loop being parallel to the sides of the scan area.

The second and third rows of this figure include the magnitude of the z component of the magnetic field. In the case of the third row, however, the value of this component is inferred from the compensated values of the other two magnetic field components since

$$k_x H_x(\omega, k_x, k_y) + k_y H_y(\omega, k_x, k_y) + \gamma H_z(\omega, k_x, k_y) = 0 \tag{8}$$

in the wavenumber domain.

A more detailed comparison can be obtained from various cuts through the gray scale contour plots. For example, along the line $y = 0$, the contour plots in the leftmost column of Fig. 8 can be redrawn as ordinary line plots as shown in Fig. 9. A similar comparison can be made for middle column of Fig. 8 by considering cuts through the line $x = 0$. This comparison is shown in Fig. 10.

We will now consider probes that do not contain a closed wire loop. For simplicity these probes will be referred to as

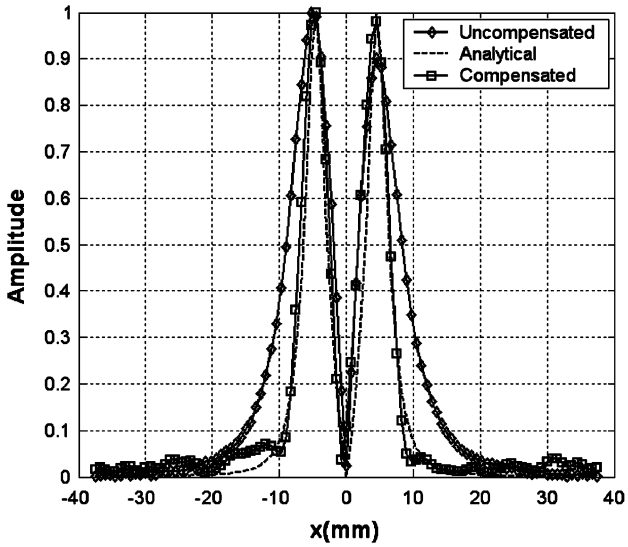

Fig. 9. A comparison of the uncompensated output for a probe ($|S_{21}|$) oriented in the x direction, the magnitude of H_x obtained from an analytical expression; and the magnitude of H_x resulting from compensation of the probe output. The y coordinate in this graph was fixed at 0.

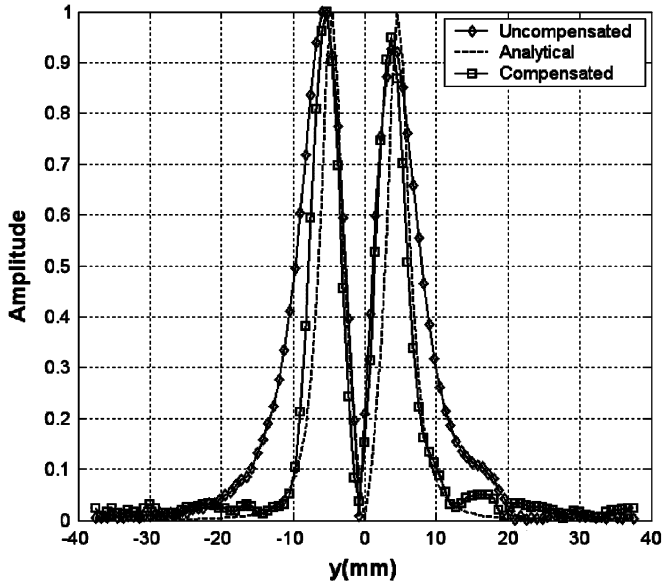

Fig. 10. A comparison of the uncompensated output for a probe ($|S_{21}|$) oriented in the y direction, the magnitude of H_y obtained from an analytical expression; and the magnitude of H_y resulting from compensation of the probe output. The x coordinate in this graph was fixed at 0.

electric field probes even though their outputs may technically be functions of both the electric and magnetic fields. The electric field probes considered in this section all consist of a segment of semirigid coaxial cable and an extended inner conductor as shown in Fig. 11(a)–(d). The probe shown in Fig. 11(c) has a curved center conductor folded back to form a small gap with the outer conductor.

These electric field probes were connected, one at a time, to port 2 of the vector network analyzer. Port 1 of the vector network analyzer was connected to the square current loop shown in Fig. 6(a) and (b) with the current loop oriented parallel to

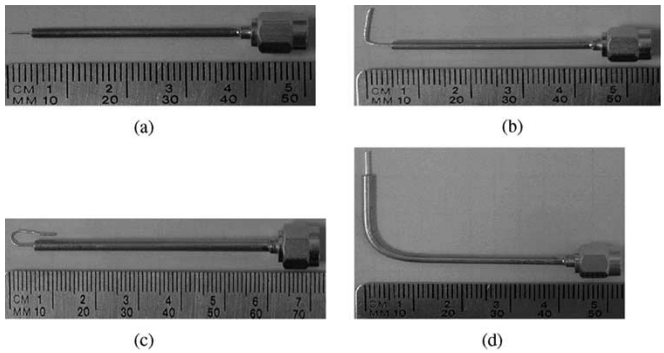

Fig. 11. Four electric field probes.

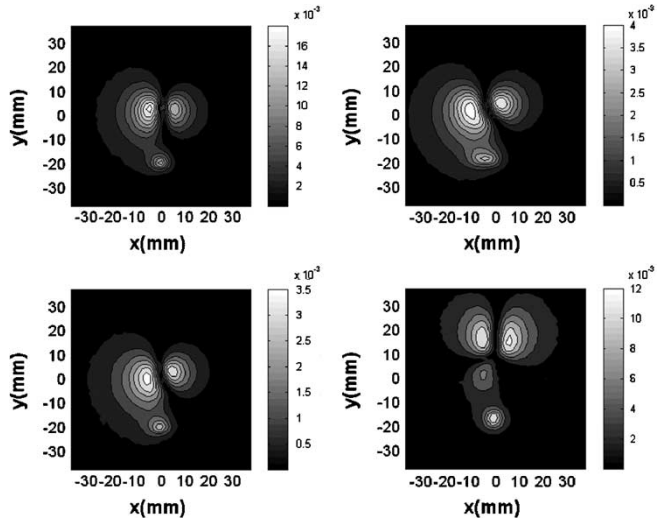

Fig. 12. The magnitude of S_{21} for the four electric field probes shown in Fig. 11. Upper left: Electric field probe (a). Upper right: Electric field probe (b). Lower left: Electric field probe (c). Lower right: Electric field probe (d).

the xy plane. Fig. 12 shows the measurements using the probes shown in Fig. 11.

In the case of electric field probes (b)–(d), the probes were oriented so that the horizontal portions of the probe were parallel to the y axis. Electric field probe (a) had no horizontal portion. It can be seen in this figure that the outputs of probes (a)–(c) are very similar. Because the horizontal segments of all four probes are zero or extremely short compared to a wavelength at 100 MHz, all probes exhibited very little sensitivity to orientation. Unfortunately, this insensitivity to orientation also made probe compensation considerably less satisfactory.

Focusing on electric field probe (d), the compensation and calibration procedures used for the magnetic field probe were also applied to the electric field probe. The objective was then to determine the magnetic field produced when the square loop of Fig. 6(a) and (b) was oriented in the horizontal plane. The uncompensated VNA measurements, the analytical predictions, and the compensated probe outputs are shown in the first, the second, and the third row of Fig. 13, respectively.

Orientations in the x and y directions for electric field probe (d) in this figure refer to whether the horizontal segment of the probe was parallel to the x axis or parallel to the y axis,

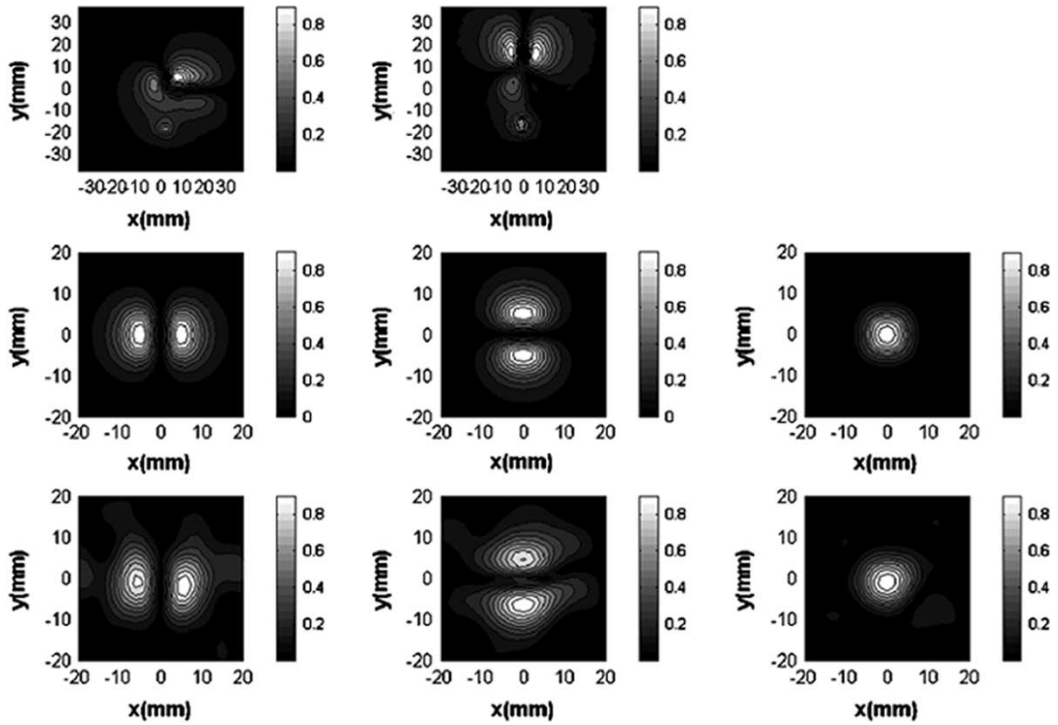

Fig. 13. Compensation results for the magnetic field components produced by a square loop using an electric field probe. Top row: Magnitude of S_{21} for electric field probe (d) oriented in the x and y directions. Middle row: magnitude of the magnetic field components in the x, y, and z directions as calculated by an analytical approximation [10]. Third row: magnitude of the magnetic field components in the x, y, and z directions determined by applying probe compensation to the measurements in the first two rows.

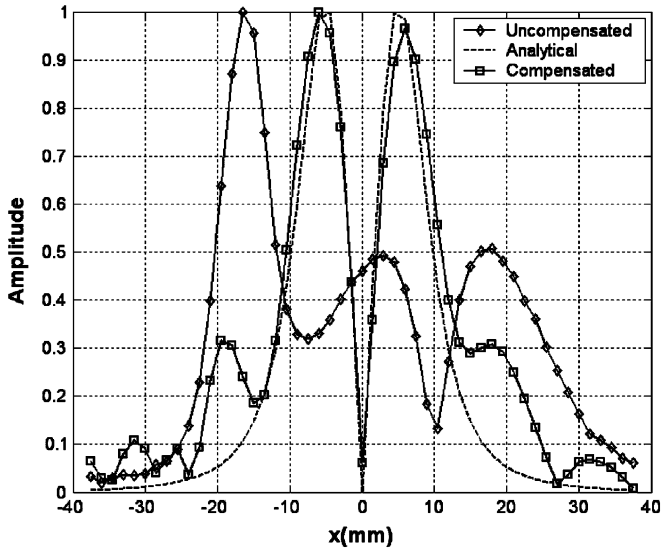

Fig. 14. A comparison of the uncompensated output for a probe ($|S_{21}|$) oriented in the x direction, the magnitude of H_x obtained from an analytical expression; and the magnitude of H_x resulting from the compensation of the probe output.

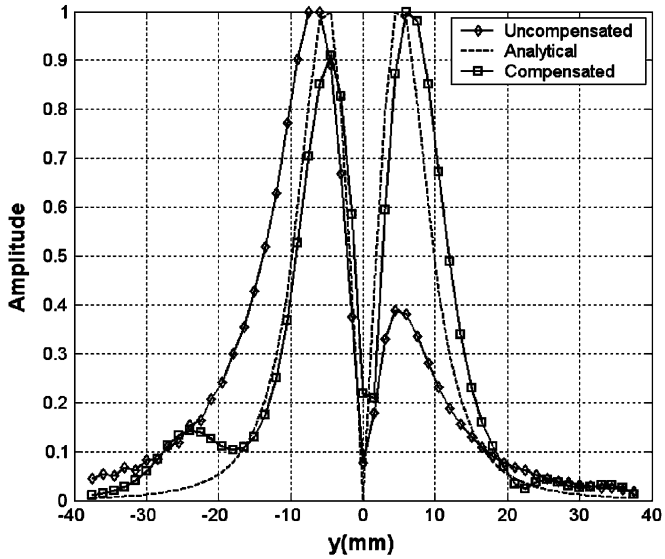

Fig. 15. A comparison of the uncompensated output for a probe ($|S_{21}|$) oriented in the y direction, the magnitude of H_y obtained from an analytical expression [10]; and the magnitude of H_y resulting from the compensation of the probe output.

respectively. Comparing this figure with Fig. 8, the resolution shown in the last two rows of the present figure is considerably lower. However, due to the differences in mechanical construction between electric field probe (d) and the magnetic field probes, the vertical standoff distance for electric field probe (d) had to be increased to 6 mm. To facilitate a detailed comparison, the contour plots in the leftmost column of Fig. 13 can be redrawn as ordinary line plots as shown in Fig. 14, for the case $y = 0$.

A similar comparison can be made for the middle column of Fig. 13 by considering cuts through the line $x = 0$. This comparison is shown in Fig. 15.

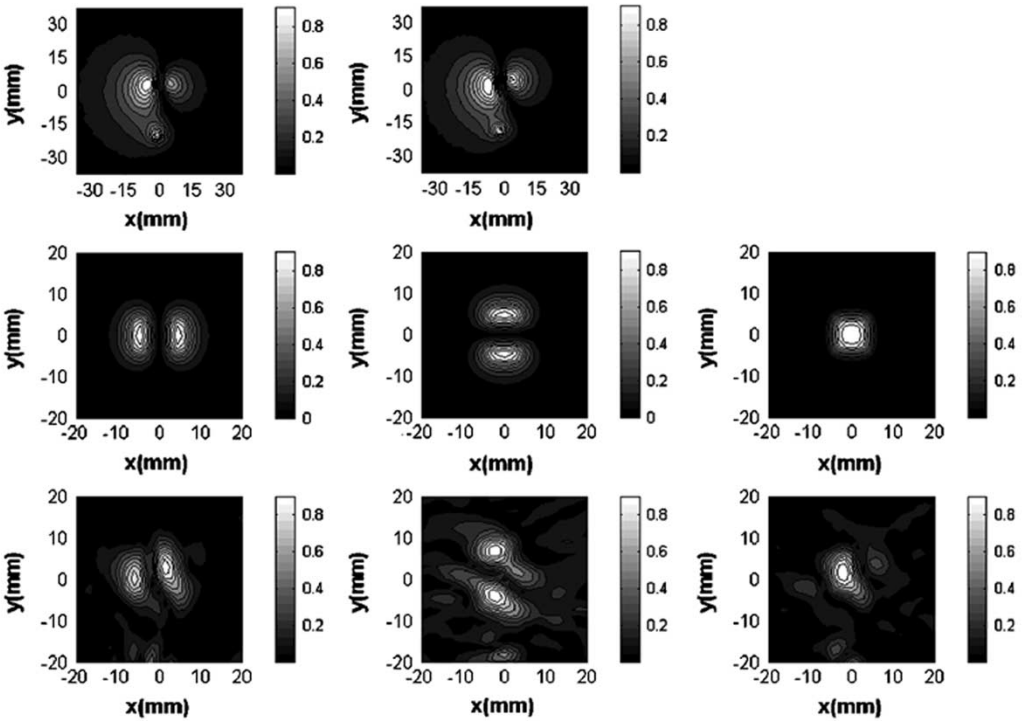

Fig. 16. Compensation results for the magnetic field components produced by a square loop using an electric field probe. Top row: Magnitude of S_{21} for electric field probe c oriented in the x and y directions; Middle row: magnitude of the magnetic field components in the x, y, and z directions as calculated by an analytical approximation [10]; Third row: magnitude of the magnetic field components in the x, y, and z directions determined by applying probe compensation to the measurements in the first two rows.

As previously mentioned the calibration and compensation procedure used for electric field probe (d) did not work as well for electric field probe (c).

As can be seen from the top row of Fig. 16, changing the orientation of probe (c) does produce a slight change in the pattern of $|S_{21}|$ as a function of position. However, the change is not nearly as significant as the change shown in the top row of Fig. 13 for electric field probe (d). This may explain why the comparison between rows 2 and 3 of Fig. 13 is much closer than the comparison between rows 2 and 3 for Fig. 16.

V. Summary and Conclusion

Near-field measurements and numerical simulations have suggested that the measurement probe does, to some degree, disturb the field it is measuring. A measurement probe having small dimensions will introduce a small disturbance to the near-field measurement and will have high spatial resolution. Both magnetic field and electric field components will contribute to the output of a measurement probe. For some cases the magnetic field may be dominant, in other cases the electric field may be dominant.

A procedure for calibration and compensation of a near-field scanning measurement for various probes was developed and described. Experimental results demonstrated that this technique can improve not only the resolution of the results obtained from magnetic field probes but also the results from electric field probes under appropriate conditions. All of the calibration and compensation procedures described were performed in the frequency domain so that this technique determines the fields one frequency at a time.

The calibration and compensation examples presented all showed some improvement in resolution when compared with the raw measurements of S_{21}. However, it should be noted that improvements in resolution may generally come at the expense of some increase in low level noise. This was demonstrated particularly by the magnetic field probe results. Since the methods proposed herein were based heavily on discrete Fourier transformations, it is important that some care must be given to specifying an adequate overall scan area and ensuring that the scan area sampling is sufficiently dense. These considerations should help to minimize the amount of low level noise introduced by these methods.

References

[1] K. P. Slattery, J. Neal, and W. Cui, "Near-field measurements of VLSI devices," *IEEE Trans. Electromagn. Compat.*, vol. 41, no. 4, pp. 374–384, Nov. 1999.

[2] R. R. Goulette, "The measurement of radiated emissions from integrated circuits," in *Proc. 1992 IEEE Int. Symp. Electromagnetic Compatibility*, Anaheim, CA, Aug. 17–21, 1992, pp. 340–345.

[3] W. Joseph and L. Martens, "The influence of the measurement probe on the evaluation of electromagnetic fields," *IEEE Trans. Electromagn. Compat.*, vol. 43, no. 2, pp. 339–349, May 2003.

[4] D. M. Kerns, "Analytical techniques for the correction of near-field antenna measurements made with an arbitrary but known measuring antenna," in *Abstracts URSI-IRE Meeting*, 1963, pp. 6–7.

[5] ——, "Correction of near-field antenna measurements made with an arbitrary but known measuring antenna," *Electron. Lett.*, vol. 6, no. 11, pp. 346–347, May 1970.

[6] ——, *Plane-Wave Scattering-Matrix Theory of Antennas and Antenna-Antenna Interactions*, Washington, DC: U.S. Government Printing Office, 1981.
[7] D. T. Paris, W. M. Leach, and E. B. Joy, "Basic theory of probe-compensated near-field measurements," *IEEE Trans. Antennas Propag.*, vol. AP-26, no. 3, pp. 373–389, May 1978.
[8] T. B. Hansen and A. D. Yaghjian, *Plane-Wave Theory of Time-Domain Fields*, Piscataway, NJ: IEEE Press, 1999.
[9] ——, "Formulation of probe-corrected planar near-field scanning in the time domain," *IEEE Trans. Antennas Propag.*, vol. 43, no. 6, pp. 569–584, Jun. 1995.
[10] J. Shi, R. E. DuBroff, K. Slattery, M. Yamaguchi, and K. Arai, "A study of the probe induced disturbances on the near-field measurement," presented at the 2003 IEEE Int. Symp. Electromagnetic Compatability, Istanbul, Turkey, 2003.
[11] G. S. Smith, *An Introduction to Classical Electromagnetic Radiation*. Cambridge, U.K.: Cambridge Univ. Press, 1997, ch. 4, pp. 262–272.
[12] P. C. Clemmow, *The Plane Wave Spectrum Representation of Electromagnetic Fields*. Piscataway, NJ: IEEE Press, 1996.

Jin Shi (S'00) was born in China in 1974. He received the B.S.E.E. degree from Central South University, Hunan, China, in 1997 and the M.S. degree in electrical engineering from Tsinghua University, Beijing, China, in 2000, and the Ph.D. degree in electrical engineering from the University of Missouri-Rolla in May 2005.

Since 2000, he has studied and worked in the Electromagnetic Compatibility Laboratory at the University of Missouri-Rolla, where his research and education have been supported by a research assistantship. Since 2002, joined Intel Corporation, Santa Clara, CA, as a Senior System Engineer in January 2005. His research interests include developing near field measurement techniques for the root cause analysis of notebook platform noise and building numerical simulation models for the notebook platforms.

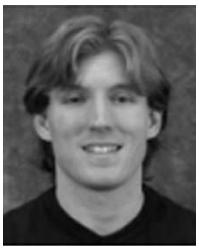

Michael Andrew Cracraft (S'96) was born in July 1978 in Jackson, MO. He received the B.S. (Summa cum laude) and M.S. degrees in electrical engineering in 2000 and 2002, respectively, from the University of Missouri-Rolla (UMR). He is currently working towards the Ph.D. degree at UMR in the Electromagnetic Compatibility Laboratory.

Mr. Cracraft is a member of Tau Beta Pi and Eta Kappa Nu.

Kevin P. Slattery (A'89–SM'98) is presently with Intel, Hillsboro, OR. His work at Intel is primarily with EMC/EMI at the silicon level, developing near field measurement techniques for scanning over processors and chipsets, and developing EMC design guidelines. In addition, he works on RF interference mitigation and high speed clocking issues.

Previously, he was with DaimlerChrysler EMC, Huntsville, AL. He has also worked in high energy physics at the Stanford Linear Accelerator Center where he was responsible for timing systems in the particle storage rings.

Masahiro Yamaguchi (M'80) received his Ph.D. degree in Electrical and Communication Engineering from Tohoku University, Sendai, Japan in 1984, and graduated from the Department of Electrical and Communication Engineering, Graduate School of Engineering, Tohoku University, Japan in 1984.

He became a Research Associate in 1984, an Associate Professor in 1991 and a Professor in 2003 at Tohoku University. His interests are in near field measurements and analysis, RF materials characterization, and ferromagnetic RF integrated devices.

Dr. Yamaguchi is a member of the IEEE EMC and magnetics societies.

Richard E. DuBroff (S'74–M'77–SM'84) received the B.S.E.E. degree from Rensselaer Polytechnic Institute, Troy, NY, in 1970 and the M.S. and Ph.D. degrees in electrical engineering from the University of Illinois, Urbana-Champaign, in 1972 and 1976, respectively.

From 1976 to 1978, he held a postdoctoral position in the Ionosphere Radio Laboratory, University of Illinois, Urbana-Champaign, and worked on backscatter inversion of ionospheric electron density profiles. From 1978 to 1984, he was a Research Engineer in the geophysics branch of Phillips Petroleum, Bartlesville, OK. Since 1984 he has been affiliated with the University of Missouri, Rolla where he is currently a Professor in the Department of Electrical and Computer Engineering.